

Structural studies on $A_2\text{ReCl}_6$ ($A=\text{K, Rb, Cs}$): absence of Jahn-Teller distortion

A. Bertin , * L. Kiefer  V. Pomjakushin  O. Fabelo  P. Becker  L. Bohatý, ⁴ and M. Braden  †

¹*II. Physikalisches Institut, Universität zu Köln, Zülpicher Straße 77, D-50937 Köln, Germany*

²*Laboratory for Neutron Scattering and Imaging, PSI, CH-5232 Villigen PSI, Switzerland*

³*Institut Laue-Langevin, 71 avenue des Martyrs 38042 Grenoble, France*

⁴*Institute of Geology and Mineralogy, Sect. Crystallography,*

University of Cologne, 50674 Cologne, Germany

(Dated: February 10, 2026)

K_2ReCl_6 belongs to the antifluorite family and exhibits a sequence of structural transitions above the onset of magnetic order at $T_N = 12$ K. Because of its $5d^3$ electronic configuration in an octahedral coordination, the ground state is a pure spin state without orbital degeneracy within the LS coupling scheme, but it can become Jahn-Teller active in the strong spin-orbit coupling limit described by the jj coupling [S. Streletsov and D. I. Khomskii, Phys. Rev. X **10**, 031043 (2020)]. While the structural transitions in K_2ReCl_6 are understood in terms of octahedral rotation and tilting, the possible impact of a Jahn-Teller distortion remains an open issue. We report on comprehensive crystal-structure studies by means of powder neutron and single-crystal x-ray diffraction on K_2ReCl_6 and on K_2SnCl_6 . The latter material is used as a reference, because it exhibits the same sequence of structural transitions as K_2ReCl_6 , but possesses a filled $4d$ shell ruling out a Jahn-Teller distortion. While the ReCl_6 octahedron in K_2ReCl_6 presents sizable distortions at intermediate temperatures, there is no such distortion persisting to low temperatures excluding a sizable Jahn-Teller effect. Studies on polycrystalline samples of Rb_2ReCl_6 and Cs_2ReCl_6 , in which the structural transitions are suppressed due to the larger alkaline ionic radius, also do not find any indications for a Jahn-Teller distortion.

I. INTRODUCTION

Many recent developments in condensed matter physics result from the interplay between strong spin-orbit coupling (SOC) and electronic correlations, and much efforts have been undertaken on heavy $4d$ and $5d$ transition-metal compounds [1–4]. For instance, Ir^{4+} can develop a spin-orbit entangled effective moment $j_{\text{eff}} = \frac{1}{2}$ with peculiar properties [5]. In the honeycomb iridates, the magnetic interaction becomes anisotropic at least approaching the fully bond-directional magnetic interaction in the Kitaev model, whose exact solution reveals a quantum-spin-liquid ground state [6]. The impact of strong SOC on other $5d$ electronic configuration has been much less studied.

With this purpose, other materials for novel spin-orbit driven phenomena are synthesized. Among the $5d$ Mott insulators K_2ReCl_6 is a promising material due to its $5d^3$ electronic configuration in a cubic crystal field. While for lighter elements, the weak SOC λ with regards to Hund's coupling J_H , is well described within the Russell-Saunders coupling scheme, the stronger SOC in heavier elements is best accounted for within the jj coupling scheme [7]. In the former case, the resulting ground state in K_2ReCl_6 would be a pure $S = \frac{3}{2}$ spin state without orbital degeneracy, while in the latter case, the resulting effective spin-orbit entangled moment would be $j_{\text{eff}} = \frac{3}{2}$ and the ground state Jahn-Teller active [8]. For transition metals in an octahedral environment, the t_{2g}

orbital degeneracy can be lifted through the coupling with vibration modes, namely an orthorhombic (called $Q2$ mode) and a tetragonal ($Q3$ mode) distortion [7, 9]. In the intermediate SOC range, a compressed ReCl_6 octahedral geometry would be stabilized, but for larger λ , the Jahn-Teller distortion amplitude is reduced [8]. This situation is reminiscent of the $A_2\text{TaCl}_6$ antifluorite compounds with a $5d^1$ electronic configuration [10], where a cubic to tetragonal transition occurs. The elongated octahedral geometry is stabilized in the case of K_2TaCl_6 , while a compressed one is stabilized for Rb_2TaCl_6 and Cs_2TaCl_6 . The latter case is expected in the case of a $5d^1$ electronic configuration and a linear Jahn-Teller distortion [8]. However, authors of Ref. [11] pointed out that anharmonic effects, expected to be stronger for the smaller K ion than for Cs and Rb ions, could restore the elongated octahedral geometry, similarly to the e_g case in half-doped manganites [12]. Furthermore, density functional theory (DFT) calculations emphasize that the tetragonal $Q3$ mode, in particular its sign, is the key to stabilize either a pure $S = \frac{1}{2}$ or a spin-orbit entangled $j_{\text{eff}} = \frac{3}{2}$ ground state in the $4d^1$ Nb antifluorite compounds; and tuning the tetragonal distortion via epitaxial strain would induce a quantum phase transition between these two ground states [13].

In K_2ReCl_6 , the Hund coupling J_H is expected to be comparable to the strength of the SOC, and therefore the jj coupling scheme can possibly apply. For instance, in the case of the double perovskite Ba_2YReO_6 (Re^{5+}), RIXS experiments reveal $J_H < \lambda$ [14], and in $\text{Ba}_2\text{MgReO}_6$, while the electronic correlations drive the charge quadrupolar order, the associated Jahn-Teller distortion plays a crucial role in the ground state stabiliza-

* bertin@ph2.uni-koeln.de

† braden@ph2.uni-koeln.de

tion [15]. On the other side, recent RIXS experiments on K_2ReCl_6 yield a ratio $\lambda/J_H \approx 0.6$, which in the theory of reference [16] is not large enough to induce a sizable Jahn-Teller distortion [17], but the interplay between the Jahn-Teller effect and the structural phase transitions was left open. Also recent DFT calculations reveal a small Jahn-Teller distortion only when enhancing the SOC beyond the self-consistent value [18].

K_2ReCl_6 belongs to the antifluorite family and undergoes a series of structural transitions at $T_t = 111\text{ K}$, $T_{m1} = 104\text{ K}$, and $T_{m2} = 76\text{ K}$ towards a tetragonal phase with space group $P4/mnc$, a first monoclinic phase with space group $C2/c$, and a second monoclinic phase with space group $P2_1/n$, respectively [20–28]. Throughout this work we use the space-group symbols to label these phases. These structural phase transitions are understood in terms of rotation and tilt of the $ReCl_6$ octahedrons (see illustrations in Fig. 1) and arise from bond-length mismatch similar to the analogous transitions in perovskites [29]. At $T_N=12\text{ K}$, AFM long-range magnetic order sets in, associated with a weak structural distortion [26–28]. However, the structural phase transitions severely impede the crystallographic analysis and so far no precise determination of the structural parameters was reported for this material. Therefore, it remains unclear whether there is a Jahn-Teller distortion driven through SOC in K_2ReCl_6 and how these structural distortions interfere with the rotation and tilting of the octahedron. The large rotation and tilting angles in the distorted low-temperature phases of K_2ReCl_6 make it more difficult to answer this question, because such distortions can induce a purely structural deformation of the transition-metal ligand octahedron, as it is observed in various perovskites [7, 30]. In order to distinguish electronically and structurally driven octahedron deformations studying an isostructural compound with a completely filled d shell appears most promising. K_2SnCl_6 exhibits the same sequence of structural phase transitions as K_2ReCl_6 [31, 32], and as it has a fully occupied $4d^{10}$ electronic configuration, there is no Jahn-Teller effect rendering it an ideal reference compound.

With the aim to identify or exclude a Jahn-Teller driven structural distortion in A_2ReCl_6 ($A=K, Rb, Cs$), we report comprehensive single-crystal x-ray diffraction (SXD) and high-resolution powder neutron diffraction (PND) measurements on K_2ReCl_6 and on K_2SnCl_6 in Sec. III, where stoichiometry, local disorder, and the characterization of the low-temperature structural phases will be discussed. We also analyze the triclinic distortion accompanying the onset of magnetic order in K_2ReCl_6 . In section IV we discuss the possible Jahn-Teller effect by comparing the crystal structure results for K_2ReCl_6 and K_2SnCl_6 . The absence of octahedral distortions at low temperature and the similar effects in both compounds in the intermediate structural phases let us conclude that the Jahn-Teller effect is essentially inactive in K_2ReCl_6 , although non-relaxed rotations and tilts can deform the structure. In Sec. IV we report on studies

on polycrystalline samples of Rb_2ReCl_6 and Cs_2ReCl_6 , in which monovalent K^+ ions are replaced by larger Rb^+ and Cs^+ ions. Also in these materials we find no indication for a Jahn-Teller distortion.

II. EXPERIMENTAL

A. Synthesis and characterization

Single crystals of K_2ReCl_6 and K_2SnCl_6 were grown from HCl solution by controlled slow evaporation of the solvent [28, 29]. A commercial K_2ReCl_6 powder was purchased from Alfa Aesar, and we crushed single crystals to obtain a powder K_2SnCl_6 sample. Detailed macroscopic measurements characterizing the structural and magnetic phase transitions in our K_2ReCl_6 crystals are described in Ref. [28]. Measurements of the magnetization at 0.1 T of the powder K_2ReCl_6 sample using a quantum design MPMS-XL7 superconducting quantum interference device magnetometer indicated a Néel temperature of $11.8(4)\text{ K}$ in perfect agreement with the single-crystal studies [28].

Powder samples of Rb_2ReCl_6 and Cs_2ReCl_6 were obtained by reaction of a solution of commercial K_2ReCl_6 with solution of $RbCl$, respectively $CsCl$, in diluted HCl. The precipitated microcrystalline Rb_2ReCl_6 , respectively Cs_2ReCl_6 , was washed several times with diluted HCl and dried. Powder x-ray diffraction experiments as a function of temperature were performed in Bragg-Brentano geometry on a *Stoe* diffractometer using $Cu K_{\alpha,1}$ radiation revealing pure phases. Samples were mounted in a He evaporation cryostat and a small amount of Si powder was mixed with the sample to determine temperature dependent instrumental parameters in particular the small sample displacement perpendicular to the sample surface. Magnetic properties of both compounds were measured using a quantum design MPMS-XL7 superconducting quantum interference device (SQUID) magnetometer.

B. SXD experiments

SXD measurements were performed in a temperature range $30\text{ K} \leq T \leq 300\text{ K}$ on a Bruker single-crystal diffractometer D8-Venture at the University of Cologne with Mo K_{α} radiation, $\lambda = 0.71\text{\AA}$, and on a D8-Venture at the Institut Laue-Langevin (ILL) with Ag K_{α} radiation, $\lambda = 0.56\text{\AA}$. Note that the use of a shorter wavelength reduces the x-ray absorption. Samples were mounted using Cargille oil on a Mitegen cryoloop. Integration was performed with the *Apex4* software. Absorption correction and scaling were performed with the *Multiscale* algorithm. The sample sizes were described by a parallelepiped with dimensions reported in the supplemental material [33]. The D8-Venture diffractometers use a microfocus x-ray source equipped with multilayer optics,

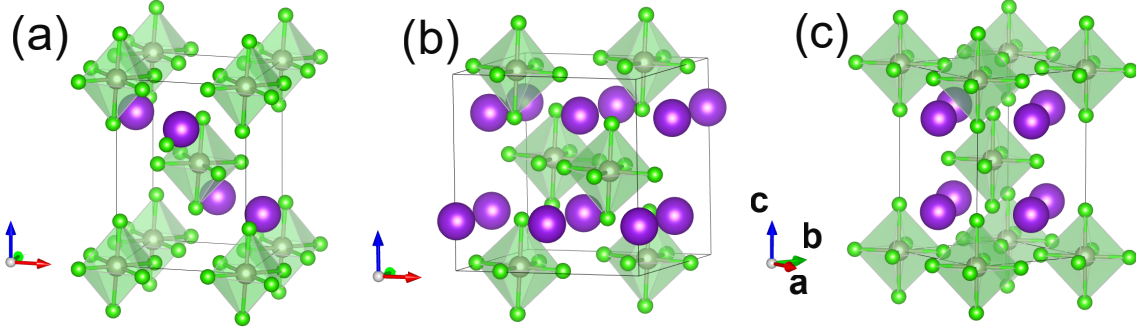


FIG. 1. Crystal structure of K_2ReCl_6 in the three low temperature phases as determined with PND. Panel (a) shows the structure at 15 K in the monoclinic $P2_1/n$ phase. Panel (b) presents the monoclinic $C2/c$ phase at 90 K. In these two monoclinic phases staggered rotation occurs around the c_m axis and the in-phase tilt around the monoclinic b_m axis that, however, changes between the two phases. Panel (c) shows the crystal structure in the tetragonal phase with only the staggered rotation around c_{tet} . Here we show the smaller lattice corresponding to $P4/mnc$. In all panels the red-green-blue arrows indicate the orientation of the lattice, K sites are shown in purple spheres and ReCl_6 octahedrons in green. Red, green and blue arrows indicate the a , b and c lattice vectors. Pictures were drawn with the visualization software VESTA3 [19].

which monochromatize the beam and suppress higher-order harmonics. For the low temperature experiments we employed a nitrogen and a helium cryostream cooler for temperatures above and below 80 K, respectively. The quality of the collected data sets is evaluated by the internal reliability values $wR^2(\text{int})$. Refinements were carried out with *Jana2020* [34] applying an extinction correction with an isotropic Becker-Coppens formalism [35].

While data sets collected in the cubic high-temperature structure described with space group $Fm\bar{3}m$ can be integrated with the cubic face-centered unit cell, data sets collected in all lower-symmetry phases were integrated with a pseudo-cubic primitive unit cell, with lattice parameter $a \sim a_{\text{cubic}}$; see Tab. S1 in the supplemental material [33]. Inherent to the symmetry reduction at the structural phase transitions, ferroelastic twin domains appear with up to 12 different orientations [28] that mimic the higher symmetry. Since the lattice distortions remain small [36] one cannot separate the contributions of individual orientations, which sometimes is even intrinsically impossible. Therefore, the integrated datasets correspond to an incoherent superposition of the up to 12 twin volumes, which was implemented in the refinements.

In the high-temperature cubic phase $Fm\bar{3}m$, the atomic displacement parameters (ADP) [37] of $Me = \text{Re}, \text{Sn}$ and K ions stay isotropic, while two anisotropic ADPs are introduced for the Cl ions: U_{\parallel} parallel and U_{\perp} perpendicular to the $Me\text{-Cl}$ bond. For the refinements in the lower-symmetry phases, the same two ADPs were refined for all Cl sites and ADPs of Me and K ions were kept isotropic. In order to calculate the bond distances and rotation and tilt angles of the octahedron, we combined the atomic positions obtained from SXD with the lattice parameters obtained from powder x-ray diffraction and documented in Ref. [28] for K_2ReCl_6 . For K_2SnCl_6 the lattice parameters are obtained from our high-resolution PND experiments. The crystal-structure

refinements yield very good reliability factors and the results are resumed in Tables S2 and S3 in the supplemental material [33].

C. PND experiments

High-resolution PND experiments were performed on the HRPT diffractometer at the SINQ neutron source of the Paul Scherrer Institute. 5.5 g of a K_2ReCl_6 sample and 5.3 g of K_2SnCl_6 sample were filled in 8 mm diameter \times 50 mm height cylindrical Vanadium sample cans that were mounted in an ILL-orange-type cryostat. A wavelength of 1.49 Å was used for both samples. K_2SnCl_6 patterns were collected in *high-intensity* mode, i.e. with a 40' primary collimator, and K_2ReCl_6 patterns were collected in *medium resolution* mode, i.e. with a 12' primary collimator. In the experiment on the K_2SnCl_6 sample for temperatures around 260 K, the determined temperature on the sample stick slightly deviated from the sample temperature, $\Delta T \sim 3$ K, due to insufficient thermalization between the sample and the sonde and is labelled T' throughout the paper. Rietveld refinements were performed with the FULLPROF program package [38]. An instrument resolution file reflecting the exact geometry of the experimental setup, modeled with a Thomson-Cox-Hastings (TCH) pseudo-Voigt function [39] convoluted with an axial-divergence asymmetry function [40], was used to describe the peak profile for K_2ReCl_6 , and a microstructure analysis has been applied. Background was modeled with a cosine Fourier series of 6th degree and an absorption correction was introduced [41][42]. For K_2ReCl_6 the powder-diffraction pattern measured in the cubic phase at 120 K was used as a reference pattern in order to determine additional instrumental parameters (zero position of the detector, the sample displacement and transparency, and one additional parameter account-

ing for the peak asymmetry). Thereafter, these parameters were fixed in the refinements with data obtained at lower temperature.

The same ADPs methodology [37] as used for the SXD analysis was applied [43]. Table I resumes the results of the PND refinements and presents the positions of the sites in the different phases.

The average apparent particle size was refined with the reference pattern at 120 K, and an almost resolution limited grain size with diameter $D = 1611.1(9)\text{\AA}$ is found for K_2ReCl_6 and fixed for all other temperatures (for K_2SnCl_6 $D = 1728(2)\text{\AA}$ is obtained with ambient-temperature data). The strain was refined for all patterns and is plotted in Fig. S1 in the supplemental material [33]. Our results indicate an almost temperature independent behavior, and the still small value inferred from the Rietveld refinement in the K_2ReCl_6 cubic phase at 120 K $e = 4.768(5) \times 10^{-4}\%$ is about five times larger than the value deduced at room temperature in K_2SnCl_6 [33].

III. TEMPERATURE DEPENDENCE OF THE CRYSTAL STRUCTURE IN K_2ReCl_6 AND IN K_2SnCl_6

A. Stoichiometry of K_2ReCl_6 and K_2SnCl_6

The stoichiometry of the investigated samples was verified using SXD data sets collected in the high-temperature phase and by keeping the site occupancy of Re fixed to one. The occupancies of the K and Cl ions are refined and are tabulated in Tab. S4 in the supplemental material [33]. With the exception of the K_2SnCl_6 crystal showing a slight excess of scattering at the Cl site, all samples do not exhibit any occupational deviation. Therefore, in the analyses described below, all occupation values were fixed to nominal stoichiometry.

B. Study of the low-temperature phases in K_2ReCl_6

The SXD data completeness, and the R -values and GOF parameters documenting the quality of the refinements, are tabulated in Tab. S1 in the supplemental material [33], and the refined atomic positions, ADPs, and twin fractions are presented in Tab. S2 in the supplemental material [33]. Because of the large number of free parameters, in particular due to the presence of twin domains in the low-temperature phases, and despite constraining the ADPs to the symmetry of the cubic parent phase, some additional constraints were applied to avoid strong correlations ($> 90\%$) between refined parameters. In all refinements in the tetragonal phase, we fix the ADP $U_{\parallel\parallel}(\text{Cl})$ to a value linearly scaled from the value found in the cubic phase at 120 K for samples #S2 and #S3. This allows us to refine the vol-

umes of the three domains, which are found to be nearly equipopulated for all samples. In the $C2/c$ phase, a constraint between the split K atomic positions is applied ($y(\text{K}_2) = y(\text{K}_1 - 0.5)$) for sample #S2 in the refinements at 90 K. Finally, for sample #S2 at 80 K, applying a resolution cut-off $\sin(\theta)/\lambda = 0.9\text{\AA}^{-1}$ is enough to suppress any strong correlation.

K_2ReCl_6 undergoes a first structural transition towards a tetragonal phase with space group $P4/mnc$. Refinements are carried out with the non-standard notation $C4/mcg$ space group, which preserves the cubic unit cell of about 10\AA length. The cubic-to-tetragonal transition corresponds to a rotation of the ReCl_6 octahedron around the tetragonal axis that is parallel to a Re-Cl bond. The rotation senses (clockwise or anticlockwise) are equal within any plane perpendicular to the c axis but the staggering is anti-phase parallel to it. Therefore, this distortion is associated with a mode at the Brillouin-zone boundary (X mode of the $Fm\bar{3}m$ cell) and breaks translation symmetry [28]. The rotation angle, ϕ , is calculated from the atomic positions of the Cl_1 and Cl_2 sites defining the octahedral basal plane (perpendicular to c). Note that Cl_1 and Cl_2 are symmetry related in $P4/mnc$ but not in $C2/c$ and $P2_1/n$. In the two monoclinic phases, the rotation angle ϕ is determined as the average of the rotations calculated using the two inequivalent basal Cl_1 and Cl_2 sites. The transition from tetragonal to the first monoclinic phase $C2/c$ is associated with the rotary phonon mode softening at the Brillouin zone center (Γ mode): an in-phase octahedral tilt against the monoclinic axis b_{m1} , where b_{m1} is parallel to a cubic [100] direction. Throughout this article we distinguish "rotation" and "tilt" for the c and \mathbf{a}, \mathbf{b} axes, respectively. We determine the tilt angle θ by averaging the values calculated using the apical Cl_3 ion and the basal Cl_1 ion sitting on the a_{m1} axis. In the second monoclinic phase $P2_1/n$, the tilt axis changes to b_{m2} parallel to a [110] cubic axis. The new tilt angle $\theta = \theta_{\text{basal}}$ is estimated from the average tilt angles of the two basal Cls. The tilt $\theta = \theta_{\text{apical}}$ is also calculated from the the apical Cl_3 ion, but differs only very little from θ_{basal} . These octahedral rotation and tilt angles are plotted against temperature in Fig. 2.

The monoclinic low-temperature phases of K_2ReCl_6 thus combine a rotation and a tilt distortion with distinct stacking schemes, which resembles the GdFeO_3 structure type that is observed in numerous perovskite oxides and that permits various distortions [7, 30, 44]. The complexity of the low-temperature $P2_1/n$ structure in the antifluorites K_2ReCl_6 and K_2SnCl_6 is, however, considerably enhanced compared to the GdFeO_3 structure type, because the in-plane Cl sites split. The antifluorites can be considered as double perovskites $A_2BB'X_6$ with an empty B' site, which represents a symmetry lowering compared to an ideal perovskite. Therefore, the tilting emerging out of the tetragonally distorted structure generates more degrees of freedom. Besides the main tilting that is in-phase

TABLE I. Structural parameters inferred from Rietveld refinements with PND data on K_2ReCl_6 (upper part) and on K_2SnCl_6 (lower part) measured in the cubic $Fm\bar{3}m$, in the tetragonal $P4mnc$, in the first monoclinic $C2/c$ and in the second monoclinic $P2_1/n$ phases. Atomic positions in the $C2/c$ phase are corrected for the origin shift $(\frac{1}{4}, \frac{1}{4}, 0)$. K_2ReCl_6 data at 14 K and 12 K are very similar to the ones at 15 K and not reported in this table for clarity. R_p , R_{wp} , and R_{exp} are the profile, weighted-profile, and expected profile R factors corrected for background and expressed in %. χ^2 denotes the goodness of fit (GOF). T' refers to the measured temperature in the experiments on K_2SnCl_6 . All ADPs U are given in \AA^2 , lattice angles in degrees and lattice constants in \AA . The structural parameters determined by single-crystal diffraction can be found in the supplemental material [33].

T	120 K K_2ReCl_6 $Fm\bar{3}m$	107 K $P4/mnc$	90 K $C2/c$	15 K $P2_1/n$	1.5 K $P_{S\bar{1}}$
$a \alpha$	$a_c=9.7629(1)$	$a_t=6.89512(3)$	$a_{m,1}=9.72660(7)$	$a_{m,2}=6.87995(4)$	$a_t=6.8789(3) \alpha_t=89.986(3)$
$b \beta$			$b_{m,1}=9.76112(9) \beta_{m,1}=90.043(2)$	$b_{m,2}=6.85975(3) \beta_{m,2}=90.102(7)$	$b_t=6.8564(3) \beta_t=90.110(1)$
$c \gamma$		$c_t=9.77059(9)$	$c_{m,1}=9.77322(9)$	$c_{m,2}=9.77919(5)$	$c_t=9.78321(4) \gamma_t=89.916(3)$
$U_{iso}(\text{Re})$	0.0056(2)	0.004(3)	0.0055(3)	0.0021(2)	0.0017(2)
K	$(\frac{1}{4}, \frac{1}{4}, \frac{1}{4})$	$(\frac{1}{2}, 0, \frac{1}{4})$	$(\frac{1}{4}, 0.266(1), \frac{1}{4}) / (\frac{1}{4}, -0.245(2), \frac{1}{4})$	0.5044(8), 0.9843(7), 0.2509(10)	0.5051(7), 0.9842(6), 0.2492(7)
$U_{iso}(\text{K})$	0.0200(4)	0.0168(6)	0.0118(10)	0.0099(5)	0.0095(4)
Cl_1	0.24024(5), 0.0	0.2426(4), -0.2344(4), 0	0.2415(3), -0.0133(3), -0.0134(4)	0.2606(2), -0.2214(2), -0.0157(2)	0.2605(2), -0.2208(2), -0.0158(2)
Cl_2	0, x , 0	$-y, x, 0$	0.0108(4), 0.2398(3), -0.0032(8)	0.2207(2), 0.2616(2), -0.0108(2)	0.2212(2), 0.2614(2), -0.0110(2)
Cl_3	0, 0, x	0, 0, 0.2428(3)	0.0153(3), -0.0002(5), 0.2406(4)	0.0271(2), -0.0011(3), 0.2400(2)	0.0271(2), -0.0012(3), 0.2397(1)
$U_{\parallel}(\text{Cl})$	0.0094(3)	0.0069(3)	0.0071(5)	0.0036(1)	0.0039(3)
$U_{\perp}(\text{Cl})$	0.0272(2)	0.0295(3)	0.0192(3)	0.0091(2)	0.0081(2)
R_p, R_{wp}	9.65 8.01	12.9 11.2	10.1 9.65	6.78 7.23	4.87 5.39
R_{exp}, χ^2	5.52 2.1	5.12 4.8	5.32 3.3	4.79 2.3	3.02 3.19

T'	255 K K_2SnCl_6 $C2/c$	160 K $P2_1/n$	40 K $P2_1/n$	1.5 K $P2_1/n$
a	$a_{m,1}=9.9586(3)$	$a_{m,2}=7.0181(1)$	$a_{m,2}=6.98310(6)$	$a_{m,2}=6.98098(6)$
b	$b_{m,1}=9.9722(3)$	$b_{m,2}=7.0117(1)$	$b_{m,2}=7.01198(5)$	$b_{m,2}=7.01398(5)$
c	$c_{m,1}=10.0123(2)$	$c_{m,2}=9.9848(5)$	$c_{m,2}=9.92215(9)$	$c_{m,2}=9.91774(9)$
β	$\beta_{m,1}=90.053(6)$	$\beta_{m,2}=90.202(2)$	$\beta_{m,2}=90.341(1)$	$\beta_{m,2}=90.3534(7)$
$U_{iso}(\text{Sn})$	0.0191(9)	0.0121(8)	0.0048(5)	0.0025(5)
K	$(\frac{1}{4}, 0.270(3), \frac{1}{4}) / (\frac{1}{4}, -0.242(3), \frac{1}{4})$	-0.011(1), 0.4728(9), 0.2502(15)	-0.0093(6), 0.4625(5), 0.2515(7)	-0.0098(7), 0.4621(5), 0.2520(7)
$U_{iso}(\text{K})$	0.039(2)	0.021(1)	0.0083(7)	0.0065(7)
Cl_1	0.2424(7), -0.0219(13), -0.0151(8)	0.2708(5), -0.2128(6), -0.0214(4)	0.2749(2), -0.2076(3), -0.0271(2)	0.2756(2), -0.2074(3), -0.0277(2)
Cl_2	0.0212(13), 0.2405(7), -0.0037(16)	0.2096(5), 0.2741(6), -0.0186(4)	0.2060(2), 0.2772(2), -0.0222(2)	0.2057(2), 0.2765(2), -0.0228(2)
Cl_3	0.0134(8), -0.0019(9), 0.2406(4)	0.0423(4), 0.0007(6), 0.2409(2)	0.0505(2), 0.0014(3), 0.2418(1)	0.0505(2), 0.0007(3), 0.2422(2)
$U_{\parallel}(\text{Cl})$	0.0220(9)	0.0132(2)	0.0046(2)	0.0049(2)
$U_{\perp}(\text{Cl})$	0.0551(8)	0.0269(4)	0.0090(2)	0.0054(4)
R_p, R_{wp}	15.1 11.7	9.84 9.67	6.45 7.15	6.81 7.56
R_{exp}, χ^2	10.6 1.22	8.42 1.32	6.65 1.16	6.12 1.53

at all sites and that occurs around the monoclinic b_{m1} and b_{m2} axes in the two distinct monoclinic phases, tilting is also possible around a_{m1} and a_{m2} , respectively. This tilting exhibits the same staggering as the rotation around c . These tiltings, however, are found to be smaller than 1° at all temperatures, supporting our assignment of the main octahedral rotation schemes across all structural transitions.

In the tetragonal phase, the rotation angle ϕ amounts to about 1° , which disagrees with the order parameter deduced from nuclear quadrupole resonance (NQR) measurements, i.e. $\phi \approx 3^\circ$ [45], but explains the weak superstructure reflections documented in Ref. [28]. The weak distortion also explains the necessity to constrain the refinement model in order to suppress the strong persistent correlation. The rotation angle ϕ increases continuously across the different structural phases up to $\phi = 4.7(1)^\circ$ at the lowest temperature, see Fig. 2(a). The discontinuity of the tilt angle θ at 104 K would suggest a first-order character of the structural transition from the tetragonal $P4/mnc$ phase to the first monoclinic $C2/c$ phase but

dense data close to this transition are lacking. We found a little temperature dependent angle of $\theta \approx 4^\circ$ in the $C2/c$ and $P2_1/n$ monoclinic phases.

The temperature dependencies of the two Cl ADPs and of the isotropic ADPs of Re and K are plotted in Fig. 2 as a function of temperature. First, there is a good agreement between the ADPs determined with the SXD data on four different samples and the PND results. As commonly observed in the antifluorite materials [29], we found at high-temperatures $U_{\parallel} \ll U_{\perp}$ and quite large U_{\perp} values. However, all ADPs shrink with temperature following mainly a linear behavior. The Cl ADPs become almost isotropic at the lowest temperature, indicating that the large high-temperature U_{\perp} value has mainly a dynamical origin. Note however, that prior to the first cubic to tetragonal transition, U_{\perp} deviates from the expected linear behavior, before significantly shrinking in the monoclinic phase $C2/c$.

PND patterns were collected in each of the crystallographic phases; see Tab. I for the results of Rietveld refinements. The lattice parameters are reported in Fig. S2

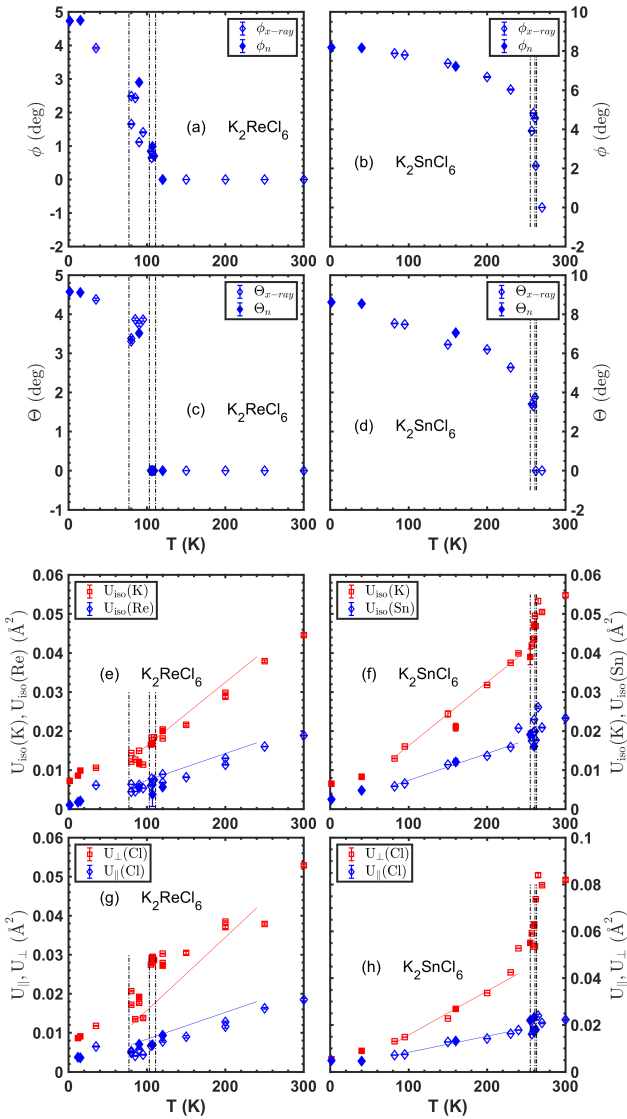


FIG. 2. The average octahedral rotation angle ϕ , as defined in the main text, is given in panel (a) for K_2ReCl_6 , and in (b) for K_2SnCl_6 . Tilt angles θ are shown in panels (c) and (d). Note that in the $P2_1/n$ phase, the tilt axis is no longer parallel to a cubic [100] but parallel to cubic [110]. Panels (e) to (h) present the ADPs for the Re (left) and Sn (right) compounds. For K and Re/Sn the ADP is isotropic (e,f), while for Cl the two ADPs U_{\parallel} and U_{\perp} are given in (g,h). The vertical dashed black lines indicate the structural transitions at $T_t = 111$ K and $T_{m1} = 103$ K, and $T_{m2} = 77$ K for K_2ReCl_6 , and at $T_t = 263$ K, $T_{m1} = 260$ K, and $T_{m2} = 255$ K for K_2SnCl_6 . The solid lines are linear fits, used as a guide to the eye. Open and filled symbols refer to SXD or PND measurements, respectively.

in the supplemental material [33], and are compared with x-ray diffraction data reproduced from Ref. [28], showing good agreement, even though the c lattice parameter may be slightly underestimated by the neutron data in the intermediate monoclinic phases. The PND data allow us to

verify that the signs of tetragonal or monoclinic splittings in the low-temperature phases were correctly attributed, see the discussion in the supplemental material [33]. This is not trivial as the local distortion of the octahedron can overcompensate the effect of rigid octahedral rotation even in the case of corner-sharing perovskites [44].

The ADPs and octahedral rotation/tilt angles deduced from PND Rietveld analysis are tabulated in Tab. I and plotted together with SXD results in Fig. 2, showing a good agreement between the two techniques.

C. Possible local disorder in K_2ReCl_6

Raman scattering experiments show already at room temperature a violation of the cubic selection rules, and the persistence of a continuum across all structural transitions down to 5 K. These observations were interpreted as the signature of octahedral rotational disorder breaking the local cubic symmetry [46]. SXD experiments analyzing integrated Bragg reflection intensities determine the average long-range crystal structure, but nevertheless local disorder or local distortion possess a measurable impact. The local disorder adds to the temperature-dependent phonon contribution to the ADPs and must lead to unusually large values [29, 47, 48]. Pronounced disorder in the high symmetry phase must even change the probability density from a 3D Gaussian distribution to functions with several or extended maxima that can be described by higher polynomials [49], as it has been demonstrated for the ferroelectric phase transition in $\text{K}(\text{H}/\text{D})_2\text{PO}_4$ [50].

In the $A_2\text{MeX}_6$ antifluorite compounds, strongly anisotropic ADPs of the X ion are a common feature: $U_{\parallel} \ll U_{\perp}$ [29]. This purely dynamical feature arises from the peculiar arrangement allowing for almost independent local rotations in $A_2\text{MeX}_6$ and is a hallmark of the rotational instability in the antifluorite family [29].

SXD measurements in the cubic $Fm\bar{3}m$ phase have been performed for K_2ReCl_6 (sample #S1 at 250 K, 200 K, and 150 K; samples #S2 and #3 at 120 K) see Tab. S1 in the supplemental material [33], and the results of refinements carried out with both harmonic and anharmonic ADPs are compared in Tab. S5 in the supplemental material [33]. The anharmonic refinements improve only very little the R -values at all temperatures, and do not lead to a significant reduction of $U_{\perp}(\text{Cl})$, see Tab. S5 in the supplemental material [33]. Also refinements of a so-called split model [50], in which the Cl position is displaced perpendicular to the lattice axes, do not yield a significant improvement of the description [33], which is exceptionally good as indicated by the very low reliability factors. T

In conclusion, refinements with anharmonic ADPs in the cubic phase do not indicate the presence of strong rotational disorder in K_2ReCl_6 at any temperature in the cubic phase. Furthermore, at low-temperature the Cl ADP transversal to the bond, U_{\perp} [see Fig. 2(g)], is

much smaller than the square of the static displacement of the Cl due to the rotation. This documents well defined long-range rotational distortions with only a minor role of local disorder that, however, for such ferroelastic phase transitions always exists due to the domain walls. As it is discussed in reference [29] for osmates and iridates, also the large ADPs in K_2ReCl_6 stem mostly from the peculiar dynamics of the materials with soft phonons spread over a large part of the Brillouin zone.

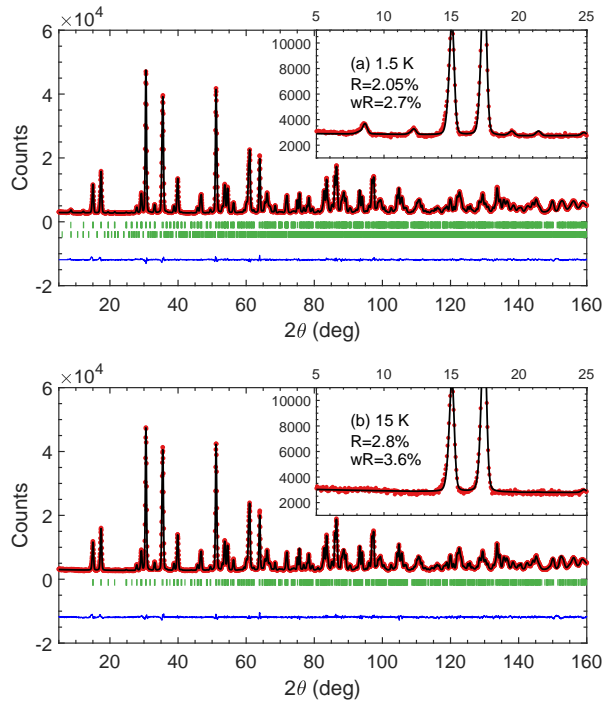


FIG. 3. High-resolution PND patterns measured on K_2ReCl_6 , (a) in the triclinic antiferromagnetic phase at $T = 1.5$ K and (b) at $T = 15$ K in the monoclinic $P2_1/n$ phase. The red circles indicate the experimental data points, the solid black lines illustrate the Rietveld refinements with monoclinic space group $P2_1/n$ (b) , and with both a triclinic nuclear phase in space group $P\bar{1}$ and a magnetic phase described in $P_S\bar{1}$ (a). The corresponding Bragg-peak positions are indicated by the green markers. The blue curve denotes the difference between the fit and the experimental data. In the panels we give the R values corrected for background and the insets present a zoom on the low-angle part, where magnetic Bragg peaks are most prominent.

D. Triclinic structural phase in the antiferromagnetic state

K_2ReCl_6 undergoes a magnetic transition at $T_N = 12$ K to a long-range AFM order described by the triclinic magnetic subgroup $P_S\bar{1}$ [28]. The small discontinuity observed at T_N in a thermal expansion measurement by dilatometry is a hint for a symmetry-lowering structural phase transition expected to occur at the onset of

magnetic order [28].

A Rietveld analysis with a reference data set measured at 15 K is shown in Fig. 3 and the refined structural parameters are given in Tab. I. The insets in Fig. 3 present the emergence of the magnetic Bragg peaks that can be easily resolved with these high-resolution data. The magnetic structure is described with the magnetic propagation vector $\mathbf{k}_{\text{mag}} = (\frac{1}{2}, \frac{1}{2}, 0)$ with regards to the monoclinic unit cell $P2_1/n$ [28]. Following the group-subgroup analysis, the maximum magnetic subgroup is $P_S\bar{1}$ with the following unit cell transformation $\mathbf{a}_{\text{tri}} = -\mathbf{a}_m + \mathbf{b}_m - \mathbf{c}_m$, $\mathbf{b}_{\text{tri}} = -\mathbf{a}_m + \mathbf{b}_m$, and $\mathbf{c}_{\text{tri}} = 2\mathbf{b}_m$ [51]. The breaking of the structural symmetry elements 2_1 or n splits the atomic positions and thus induces a doubling of the number of positional parameters. Refinements with this model converge but do not yield any significant differences between these split sites due to the strongly enhanced number of parameters. Therefore, we described the nuclear structure by adding the corresponding constraints for the position parameters of sites related by symmetry in $P2_1/n$. Note, that in this refinement the octahedron can still be distorted as in the paramagnetic $P2_1/n$ phase just above the Néel temperature. We also use the same primitive lattice of $P2_1/n$ and just allow α_t and γ_t to deviate from 90° . As can be seen in Tab. I, there is almost no significant change in the positional parameters at 15 and 1.5 K, but the triclinic angles clearly deviate from 90° in the antiferromagnetic phase and there are small but significant changes in the lattice constants; see Fig. 5. The effect in γ is most pronounced, which perfectly agrees with the magnetic structure model requiring that $[0.5, 0.5, 0]$ and $[-0.5, 0.5, 0]$ become inequivalent due to the emergence of antiferromagnetic order [28]. Also the moments shown in Fig. 5(c) agree with the previous determination of the magnetic structure that was performed with higher statistics and a longer wavelength [28]. The length of the moment can be precisely determined to $1.92(9) \mu_B$ (compared to $1.98(8) \mu_B$ in reference [28]), but the estimation rotation of the moment with the a, b plane suffers from the small difference between these two monoclinic axes.

E. Crystal structure of K_2SnCl_6 as a reference material with completely filled d shell

K_2SnCl_6 crystallizes at room temperature in the cubic antifluorite structure $Fm\bar{3}m$, and exhibits a sequence of structural transitions in a narrow temperature range. First, two structural transitions have been revealed by means of powder and single-crystal neutron and x-ray diffraction experiments at 261 K towards a tetragonal phase described with space group $P4/mnc$, and at 255 K towards a monoclinic phase with space group $P2_1/n$ [31, 32]. These structural transitions support the interpretation of Raman scattering and Mößbauer spectra [52, 53]. NQR measurements also suggest two structural transitions at 262 K and 256 K, but towards

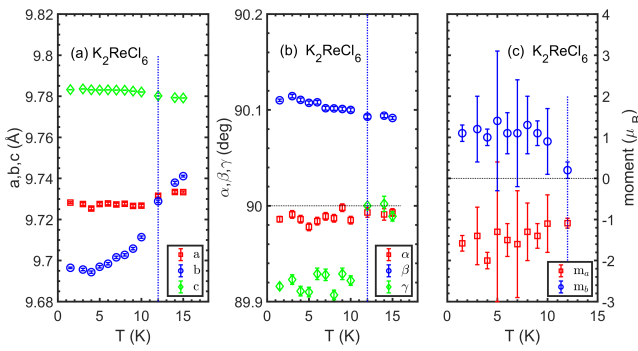


FIG. 4. Temperature dependencies of the triclinic lattice parameters a , b and c (a), of the triclinic angles α , β and γ (b) and of the ordered magnetic moments along the (almost perpendicular) directions a and b (c) that were deduced from Rietveld refinements with high-resolution PND patterns on HRPT. The magnetic transition at $T_N = 12$ K is indicated by the vertical blue dotted line.

first an orthorhombic structure and then to a monoclinic phase [54]. Investigation of x-ray diffuse scattering at room temperature suggests that the first structural transition is driven by the condensation of a soft phonon mode at the Γ point [55], similarly to early studies on K_2ReCl_6 [56, 57]. However, later, the temperature study of selected Bragg reflections by high-resolution SXD in reference [58] revealed the onset of an intermediate structural phase at 265 K, before a clear orthorhombic splitting is evidenced at 262 K, and the monoclinic structure sets in at 255 K. In reference [59] the structural sequence was then further clarified: three structural transitions occur at $T_t = 263$ K, $T_{m1} = 261$ K, and $T_{m2} = 255$ K towards a tetragonal phase with space group $P4/mnc$, a first monoclinic phase with space group $C2/c$, and a second monoclinic phase with space group $P2_1/n$. Therefore, in a narrow temperature range, K_2SnCl_6 exhibits the same sequence of structural phase transitions as K_2ReCl_6 . Due to its fully occupied $4d^{10}$ electronic configuration, the Jahn-Teller effect is not active rendering K_2SnCl_6 an ideal reference material.

In order to compare with our results on K_2ReCl_6 , SXD data have been collected in the four different crystallographic phases: at 270 K in the cubic $Fm\bar{3}m$ phase, at 262 K in the tetragonal $P4/mnc$ phase, at 261 K, 259 K, and 257 K in the first $C2/c$ monoclinic phase, and at 230 K, 200 K, 150 K, 95 K, and 82 K in the second monoclinic $P2_1/n$ phase. The data completeness, and the R -values and GOF parameters documenting the quality of the refinements are tabulated in Tab. S1 in the supplemental material [33].

Precession maps calculated in the $(h0l)$ reciprocal space plane are shown in Fig. 5 at 270 K in the cubic phase (left panel) showing the good quality of our crystal, and at 262 K in the tetragonal phase (right panel). Clear superstructure reflections of type (103), (301), (105) and

(503) indicate the breaking of the F centering and attest the presence of an intermediate tetragonal phase in a narrow temperature range, supporting the conclusions from Ref. [59]. Note also the presence of minor spurious reflections arising from a tiny additional grain.

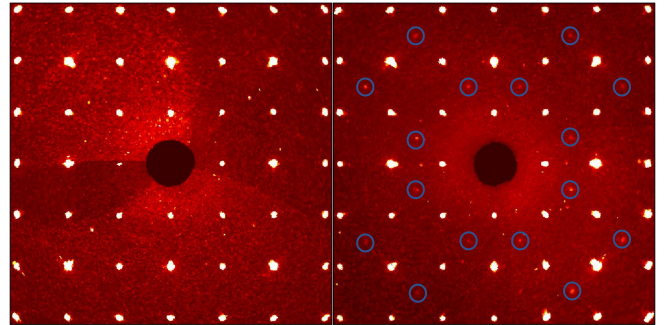


FIG. 5. Precession maps computed in the $(h0l)$ scattering plane from SXD measurements on K_2SnCl_6 at 270 K in the cubic phase (left panel) and at 262 K in the tetragonal phase (right panel). The blue circles highlight the superstructure reflections emerging in the low-symmetry phase, and breaking the F centering.

Data sets collected in the low-symmetry phases were treated as described in Sec. II. All inferred structural information are gathered in Tab. S3 in the supplemental material [33]. Note that in the two monoclinic phases, the structural model solutions describing best the data sets are not unique. This ambiguity is lifted by the Rietveld analysis of high-resolution PND data collected in both monoclinic phases: the chosen structural model solution corresponds to the choice of monoclinic angle $\beta_{m1,m2} > 90^\circ$. At 262 K, in the tetragonal phase, there is a strong correlation between $x(\text{Cl}_1)$ and $z(\text{Cl}_3)$ that cannot be suppressed by fixing $U_{\parallel}(\text{Cl})$ (to a value linearly scaled from the $U_{\parallel}(\text{Cl})$ value found at 270 K), as it was done in the tetragonal phase of K_2ReCl_6 . Note that in all subsequent refinements, no other constraints or fixed parameters are introduced, and all parameters are refined, including all twining fractions.

Since the sequence of structural phase transitions is identical to that in K_2ReCl_6 , we can directly compare the octahedral rotation/tilt angles ϕ/θ in Fig. 2(b), which includes the PND results. The increase of ϕ is consistent with a second-order phase transition, while the tilt angle θ exhibits a discontinuous increase at the first monoclinic structural transition $T_{m2} = 260$ K with $\theta = 3.6(2)^\circ$ suggesting a first-order character. Note that already in the tetragonal phase, the rotation angle $\phi = 2.23(3)^\circ$ is larger than that found in the tetragonal phase of K_2ReCl_6 , explaining the stronger superstructure reflections observed in the precession maps. The tilt and rotation angles increase continuously up to $\phi = \theta = 8.1(1)^\circ$, a value also roughly twice larger than those in K_2ReCl_6 , in line with the smaller tolerance factor calculated for K_2SnCl_6 due to the larger radius of the Sn^{4+} ion [29].

Figure 2 presents the temperature dependence of the

ADPs in K_2SnCl_6 . $U_{\perp}(\text{Cl})$ and $U_{\text{iso}}(\text{K})$ strongly shrink across the narrow temperature interval of the three structural transitions, which reflects the more abrupt emergence of the tilt and rotations distortions and points to some disorder in the cubic phase; see below. In the low-temperature phase $P2_1/n$, all ADPs follow the expected roughly linear behavior upon cooling.

For the K_2SnCl_6 SXD measurement at 270 K in the cubic phase, the anharmonic refinement with space group $Fm\bar{3}m$ yields considerable improvement of the R -values; see Tab. S5 in the supplemental material [33], and the most significant anharmonic parameter $C_{122} = C_{133}$ is much larger than that found in the Re counterpart. Furthermore, the split model yields a much stronger deviation from the cubic symmetry $y(\text{Cl}) = 0.0206(7)$, compared to K_2ReCl_6 ; see Tab. S5. This deviation of $\approx 0.2\text{\AA}$ is comparable to $\sqrt{U_{\perp}} = 0.28\text{\AA}$ deduced from the refinement with the harmonic ADPs. In addition, U_{\perp} is strongly reduced in the split model. Finally, there is a significant improvement of the R -values compared to the standard analysis with harmonic ADPs. For K_2SnCl_6 , both methods thus indicate the presence of some disorder at the Cl site in the cubic phase that may stem from a small deviation from stoichiometry; see section III.A, but note that the measurement was performed more close to the structural phase transition than in the case of K_2ReCl_6 . Local disorder in the parent phase furthermore can contribute to the more rapid emergence of the long-range rotational distortion upon cooling that is visible in Fig. 2 and 7 as well as in the literature [58]. The low ADPs of the Cl sites in K_2SnCl_6 at low temperature, however, clearly show that the low-temperature phase is well ordered and does not exhibit a significant local rotational disorder. Note, that a fully disordered rotation by about 8° would imply $U_{\perp} \sim 0.1\text{\AA}^2$ while the low-temperature experimental value is an order of magnitude smaller and consistent with dynamical zero-point fluctuations (that are thus much smaller than the static distortion).

The temperature dependencies of the lattice parameters and of the monoclinic angles, deduced from the PND Rietveld analysis, are shown in Fig. 7, which also presents a zoom into the narrow temperature range where the three structural transitions occur. A clear tetragonal splitting is resolved at $T'_t = 260\text{ K}$ indicating the transition to a tetragonal phase with space group $P4/mnc$, followed by breaking of the tetragonal symmetry and the deviation from 90° of the monoclinic angle β_{m1} at $T'_{m1} = 257\text{ K}$ marking the transition to the first monoclinic phase described with the $C2/c$ space group. Finally, the transition towards the second monoclinic phase with space group $P2_1/n$ occurs below $T'_{m2} < 252\text{ K}$. The sequence of phase transitions in our sample thus agrees with reference [59].

The tetragonal splitting and the monoclinic angles are larger in K_2SnCl_6 in agreement with the larger tilt and rotation angels. A crossing between the a_{m2} and b_{m2} happened around 120 K and was not evidenced in K_2ReCl_6 .

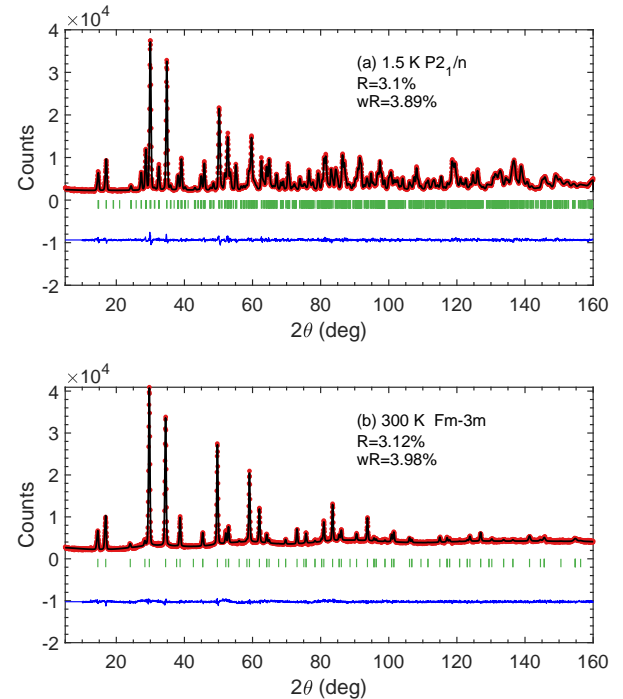


FIG. 6. Rietveld analysis of PND patterns measured on K_2SnCl_6 (a) at $T = 1.5\text{ K}$ in the monoclinic $P2_1/n$ phase and (b) at $T = 300\text{ K}$ in the cubic $Fm\bar{3}m$ phase (reference pattern). The signification of colored lines and bars corresponds to Fig. 3.

The correct assignment of the lattice parameters has been carefully tested as it is explained in the supplemental material [33].

A pattern measured at 1.5 K in the monoclinic phase $P2_1/n$ is shown in Fig. 6 and can be compared with the pattern measured at room temperature. These patterns appear quite different due to the strong structural distortions reducing the lattice symmetry and due to the large ADPs reducing the high-angle intensities in the 300 K pattern. As the high-angle part of these data further suffers from the lower resolution in these PND experiments compared to that on K_2ReCl_6 the precision of the structural parameters at higher temperature is no longer comparable to that in the SXD experiments. Therefore, only the low-temperature Rietveld results for K_2SnCl_6 are included in Fig. 2 and Fig. 8(b).

IV. ABSENCE OF JAHN-TELLER DISTORTIONS IN K_2ReCl_6 AT LOW TEMPERATURE

In order to analyze the possible presence of a Jahn-Teller distortion, the tetragonal, δ_{tet} , and orthorhombic, δ_{orth} , octahedral distortions are calculated as follows:

$$\delta_{tet} = \frac{d_3 - d_{bas}}{d_3 + d_{bas}}; \quad \delta_{orth} = \frac{d_2 - d_1}{d_2 + d_1}, \quad (1)$$

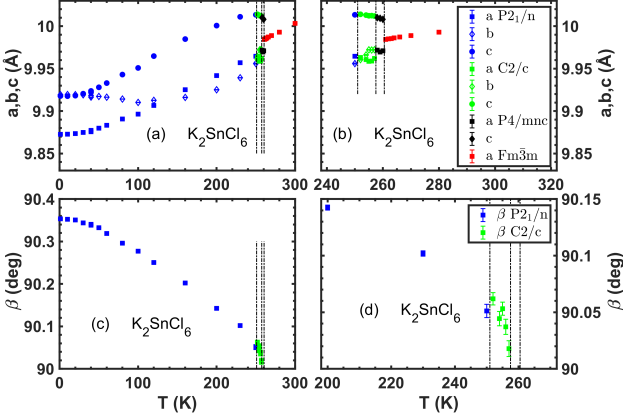


FIG. 7. Temperature dependence of the K_2SnCl_6 lattice parameters inferred from Rietveld refinements describing the PND patterns measured on HRPT. A zoom across the successive structural transitions over a narrow temperature range is shown in the right panels. The black dashed lines indicated the structural transition temperatures from our neutron powder measurements, i.e. T' not corrected for the temperature offset ΔT .

where d_i are the $\text{Re}-\text{Cl}_i$ bond distances, and $d_{bas} = (d_1 + d_2)/2$ is the average distance in the basal plane. While $d_{bas} = d_1 = d_2$ in the tetragonal phase, $d_1 \neq d_2$ in the two monoclinic phases. The octahedral distortion parameters are plotted against temperature in Fig. 8 showing good agreement between SXD and PND results.

Focusing first on the K_2ReCl_6 results shown in Fig. 8(a,c), a strong tetragonal distortion with an average value of $\delta_{tet} \approx 1.6\%$ emerges in the tetragonal phase $P4/mnc$, reaches a maximum in the first monoclinic phase $C2/c$ and decreases when approaching the transition to the second monoclinic phase $P2_1/n$. At low temperature in $P2_1/n$, SXD and PND experiments consistently yield a vanishing tetragonal distortion. A significant orthorhombic distortion $\delta_{orth} \approx 1.3\%$ emerges in the upper monoclinic phase $C2/c$, but again no sizable distortion persists at low temperature in the $P2_1/n$ phase. The presence of octahedral distortions at intermediate temperatures and their disappearance at the lowest temperatures is also visible in the plot of the three $\text{Re}-\text{Cl}$ distances in Fig. 10(a).

Figure 8(b,d) presents the temperature dependencies of the $\text{Sn}-\text{Cl}$ distances and of both octahedral distortions in K_2SnCl_6 [60]. Unlike in K_2ReCl_6 , the tetragonal distortion remains below 0.3% over the full temperature range. On the contrary, similarly to K_2ReCl_6 , in the intermediate monoclinic $C2/c$ phase, a large orthorhombic distortion $\delta_{orth} = 2.3(1)\%$ emerges at T_{m1} , and decreases towards low temperature. Upon entering in the second $P2_1/n$ monoclinic phase, the orthorhombic distortion becomes vanishingly small down to the lowest studied temperature.

In the same spirit one may analyze the $\text{Cl}-\text{Cl}$ distances

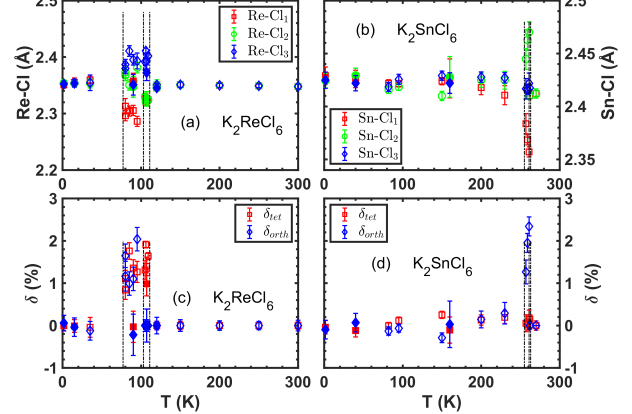


FIG. 8. Temperature dependencies of the $Me-\text{Cl}$ distances (a,b) and of the averaged tetragonal and orthorhombic octahedral distortions (c,d) as defined in the main text, for K_2ReCl_6 in panel (a,c) and for K_2ReCl_6 in (b,d). Open symbols refer to the K_2ReCl_6 SXD and to the K_2SnCl_6 SXD results and the filled symbols designate the PND analyses. Vertical dashed black lines indicate the structural transitions.

corresponding to the octahedral edges, see supplemental material [33]. In the cubic phase all edges are equivalent with a length of 3.34 Å in K_2ReCl_6 (3.41 Å in K_2SnCl_6). In the low temperature phases there can be up to six different edge lengths and at intermediate temperature one observes several splittings of the order of one percent, but at low temperature all edge lengths are nearly identical again. The absence of sizable splitting of $\text{Cl}-\text{Cl}$ and $\text{Re}-\text{Cl}$ distances implies that also the bond-angles in an octahedron do not deviate from 90°.

Summarizing the analysis of octahedral distortions, K_2SnCl_6 exhibits a sizable orthorhombic octahedral distortion in the first monoclinic phase $C2/c$ that quickly vanishes when entering the second monoclinic $P2_1/n$ phase. No tetragonal distortion is perceptible in K_2SnCl_6 across the entire temperature range. K_2ReCl_6 also exhibits sizable orthorhombic and tetragonal octahedral distortions but only in the intermediate structural phases, where it thus differs from the reference compound K_2SnCl_6 . However, in the low-temperature $P2_1/n$ phase, both octahedral distortions relax and nearly vanish also in K_2ReCl_6 . This renders an electronic or Jahn-Teller origin of the distortions very unlikely in agreement with RIXS experiments on K_2ReCl_6 [17]. The distortions appearing in the intermediate phases of both materials seem to stem from a purely structural origin. In the tetragonal and upper monoclinic phases the rotated octahedron cannot fully relax but seems to be forced into these distortions by structural constraints, which however finally disappear with the other tilting scheme in the low-temperature symmetry $P2_1/n$. The suppression of internal octahedral distortions in the low-temperature $P2_1/n$ phase contributes to the balance between the two monoclinic phases that both combine tilt and rotations.

Therefore the relaxation of octahedral deformations contributes to driving this first-order phase transition in the two materials with completely and partially filled d shells.

V. MAGNETIC ORDER AND CRYSTAL STRUCTURE IN Rb_2ReCl_6 AND Cs_2ReCl_6

It appears interesting to investigate the magnetic order and crystal structure in the related materials Rb_2ReCl_6 and Cs_2ReCl_6 , because the larger alkaline ionic radii of Rb^+ and Cs^+ imply larger tolerance factors of 1.023 and 1.069, respectively. For these tolerance-factor values, one does not expect the rotational phase transitions [29], while the electronic configuration of Re^{4+} is identical to that in K_2ReCl_6 . These two materials were very little studied: For Cs_2ReCl_6 the room temperature crystal structure in space group $Fm\bar{3}m$ and magnetic measurements above 90 K were reported [61, 62] and for Rb_2ReCl_6 only luminescence experiments were published [63, 64].

TABLE II. Magnetic properties and crystal structure parameters of Rb_2ReCl_6 and Cs_2ReCl_6 . The analysis of the SQUID magnetization measurements at 0.1 T yields the magnetic entities in the upper part, and Rietveld refinements in space group $Fm\bar{3}m$ with powder x-ray diffraction data are summarized in the lower part. Re is at (0,0,0) and Rb/Cs at $(\frac{1}{4}, \frac{1}{4}, \frac{1}{4})$ and atomic displacement parameters U are given in \AA^2 .

	Rb_2ReCl_6		Cs_2ReCl_6	
χ_0 (emu/mol)	-9.4(2)· 10^{-4}		-8.49(8)· 10^{-4}	
θ (K)	-92.7(5)		-45.5(5)	
p_{eff} (μ_B)	3.93(2)		3.79(1)	
T_N (K)	15.0(6)		9.4(6)	
T (K)	290	5	290	7
R (%)	7.5	10.1	7.4	7.9
a (\AA)	9.9738(2)	9.8684(2)	10.2578(2)	10.1510(2)
Re U_{iso}	0.0378(4)	0.0169(4)	0.0242(5)	0.0108(4)
Rb/Cs U_{iso}	0.0482(6)	0.0131(5)	0.0331(6)	0.0141(4)
Cl ($x,0,0$)	0.2462(2)	0.2489(3)	0.2425(3)	0.2444(3)
U_{11}	0.036(2)	0.004(2)	0.019(2)	0.012(2)
$U_{22}=U_{33}$	0.069(2)	0.030(2)	0.048(2)	0.028(2)

The powder x-ray diffraction data obtained with both samples at temperatures of 290 K and below 10 K are well described in space group $Fm\bar{3}m$; see Fig. 9 indicating that no structural phase transition occurs below room temperature in these two materials. For a closer inspection Fig. 10 compares the peak profiles of several Bragg reflections measured at 290 K and below 10 K, respectively. For better visibility the low-temperature data were shifted horizontally to correct for the thermal expansion. There is no change in the peak profiles, and also the fitted widths of Lorentzian distributions do not significantly change upon cooling. Therefore, we can conclude that Rb_2ReCl_6 and Cs_2ReCl_6 both do not exhibit the rotational phase transition observed in all antifluorites with a tolerance factor below ~ 1 ; see Ref. [29]. The absence of a translation-lattice distortion also renders a long-range

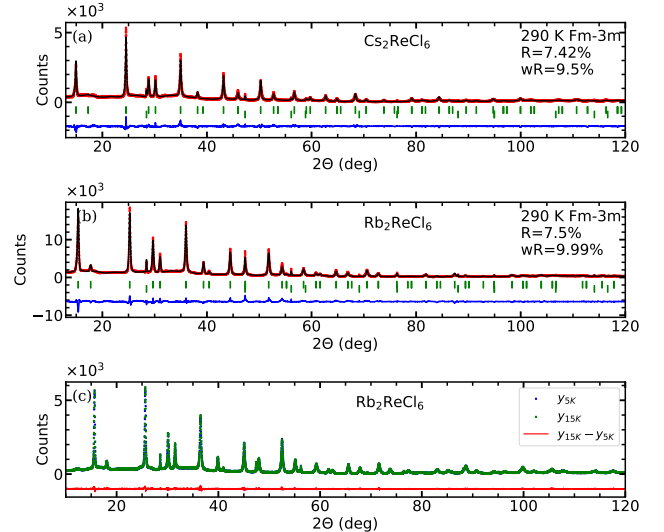


FIG. 9. Rietveld analysis of the powder x-ray diffraction patterns obtained for Cs_2ReCl_6 (a) and Rb_2ReCl_6 (b) at 290 K. The signification of colored lines and bars corresponds to Fig. 3. There are no peaks that cannot be indexed with the main phase [besides those of the admixed Si powder (lower row of green bars)]. Panel (c) compares the patterns obtained for Rb_2ReCl_6 at and below its Néel temperature of 15 K as well as the subtraction of the two patterns (red lines).

Jahn-Teller very unlikely, although it may not fully be excluded that local octahedral distortions arrange in a scheme maintaining cubic symmetry. The powder data do not permit a comparably detailed structural analysis as our measurements on K_2ReCl_6 ; nevertheless the absence of a sizable lattice distortion well agrees with the absence of the Jahn-Teller effect in K_2ReCl_6 deduced from our more precise SXD and PND studies.

The structural parameters obtained from the Rietveld analysis are summarized in Tab. II. There is agreement with the existing room-temperature data for Cs_2ReCl_6 [61]. The room-temperature cubic lattice constants increase with the atomic number and with the size of the alkaline ion. All three $A_2\text{ReCl}_6$ compounds exhibit a quite large thermal expansion with lattice-constant differences between ~ 10 and 290 K of $\Delta a=0.107 \text{\AA}$, $\Delta a=0.105 \text{\AA}$ and $\Delta a=0.096 \text{\AA}$ for the Cs, Rb and K compounds, respectively. The pronounced contraction can be attributed to the empty site of the antifluorite structure compared to a perovskite, and the smaller volume shrinking in K_2ReCl_6 results from the occurrence of the rotational phase transitions that relax internal strain similar to perovskite related compounds [65]. The Rietveld refinements find large ADPs for the A site and for the direction perpendicular to the bond at the Cl site, which indicate that the phonon modes associated with rotational transitions are also soft in these two materials.

SQUID experiments determine the magnetic properties of Rb_2ReCl_6 and Cs_2ReCl_6 ; see Fig. 11. The drop of the susceptibility at low temperature indicates the

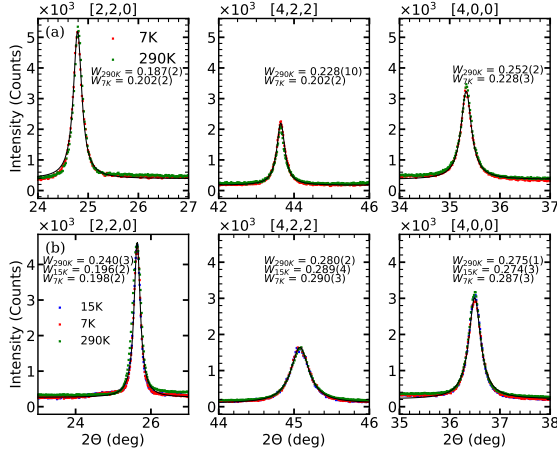


FIG. 10. Comparison of several Bragg reflection peak profiles for Cs_2ReCl_6 [upper panels (a)] and for Rb_2ReCl_6 [lower panels (b)]. For Rb_2ReCl_6 we compare 7, 15 and 290 K and for Cs_2ReCl_6 7 and 290 K. We have horizontally shifted the low-temperature data to better visualize any changes in the peak profiles. The individual peaks were fitted by Lorentzian distributions (black lines for the low-temperature data) and the differences of the width parameters are shown in the panels, but there is no significant change.

occurrence of antiferromagnetic order at $T_N=15.0(6)$ K and $9.4(6)$ K, respectively. The lower antiferromagnetic transition in the Cs compound can be attributed to the larger lattice constant inducing smaller magnetic coupling. However, both values are comparable to the $T_N=12$ K in K_2ReCl_6 , which indicates that the structural distortions of the Re compound do not lift frustration with an essential impact on the magnetic ordering. The antiferromagnetic order must essentially be stabilized by next-nearest and even farther-neighbor interactions that are not frustrated in the face-centered cubic structure.

The temperature dependence of the magnetic molar susceptibility was fitted by a Curie-Weiss law:

$$\chi(T) = N_A \frac{(p_{\text{eff}}\mu_B)^2}{3k_B(T - \theta_W)} + \chi_0, \quad (2)$$

where, N_A is the Avogadro constant, k_B the Boltzmann constant, p_{eff} the effective magnetic moment in Bohr magnetons, θ_W the Weiss temperature and χ_0 a temperature independent background. The effective moments are close to the free-fitted value obtained in K_2ReCl_6 , $3.98 \mu_B$ [28], and all three experimental moments agree within a few percent with the value expected for a pure spin $3/2$ moment, $3.87 \mu_B$, which suggests only a small impact of the spin-orbit coupling. On a mean-field level the Weiss temperature is given by $\theta_W = \sum_i \frac{1}{3} z_i J_i S(S+1)$, where J_i is the Heisenberg interaction per bond (in Kelvin) and z_i the number of neighbors. Comparing the Weiss temperatures given in Tab. II with that of K_2ReCl_6 , -112 K [28], there is no indication for particularly enhanced antiferromagnetic in-

teraction in the structurally distorted K_2ReCl_6 compound, but all three Weiss temperatures seem to follow the increase in lattice volume. The rather large values of the Weiss temperature can be understood with only moderate nearest-neighbor interaction due to the large spin moment combined with $z_1=12$. Inspecting the ratio between Néel and Weiss temperatures, there is no indication for enhanced frustration in the cubic materials.

Figure 9(c) compares the x-ray diffraction patterns obtained for Rb_2ReCl_6 at $T_N=15$ K and below in the aim to search for some splitting induced by the antiferromagnetic order that can reduce the symmetry similar to the triclinic distortion emerging in the antiferromagnetic phase of K_2ReCl_6 ; see Fig. 5. Due to the negligible thermal expansion in this temperature range we can simply subtract these two patterns [red curve in Fig. 9(c)] obtaining essentially a zero line. There are only tiny indications for peak broadening in the antiferromagnetic state.

In summary the studies of Rb_2ReCl_6 and Cs_2ReCl_6 reveal quite similar magnetic properties compared to K_2ReCl_6 , indicating that the rotational distortions do not severely impact the magnetic coupling, which seems to follow the lattice enlargement implied by the larger alkaline ions. Furthermore, the effective moments agree with the expectation for a pure spin moment in the three materials suggesting only moderate impact of spin-orbit coupling.

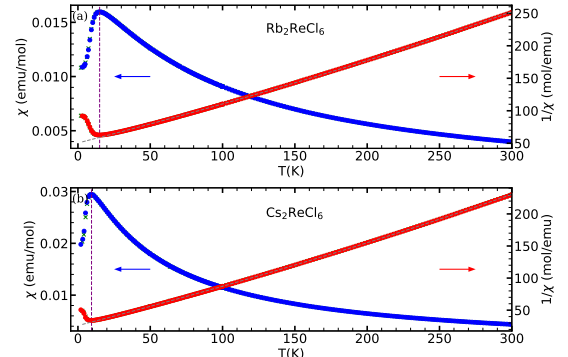


FIG. 11. Temperature dependent field-cooled susceptibility (blue) and its inverse (red) determined by SQUID measurements at 0.1 T for Rb_2ReCl_6 (a) and Cs_2ReCl_6 (b) upon heating. The susceptibility data were fitted by a Curie-Weiss law as described in the text. The green \times symbols plotted below the blue ones denote zero-field-cooled measurements but there is no difference with the results obtained upon field cooling.

VI. CONCLUSION

The two antifluorite materials K_2ReCl_6 and K_2SnCl_6 exhibit the same sequence of structural phase transitions associated with rotation and tilting of the octahedron around different axes parallel to either a $Me\text{-Cl}$ bond or

a Cl-Cl octahedron edge with either the same phase at all sites or with staggering of opposite rotation angles. Although these structural deformations resemble those observed in oxide perovskites in the GdFeO_3 structure type, the complexity in the antifluorites is larger due to the double-perovskite character with an empty B' site. This complexity impedes the search for an electronically or Jahn-Teller driven deformation of the MeCl_6 octahedron. Crystal structure investigations were performed by high-resolution PND and by SXD and agree very well with each other. The occurrence of the same sequence of structural phases in the two materials with a partially filled and a completely filled d shell documents that these transitions are not driven by electronic effects in the d shell but arise from the common bond-length mismatch that is well established for perovskites. While both materials exhibit some internal deformations of the MeCl_6 octahedron at intermediate temperatures, we find a rather ideal octahedron at low temperatures in the second monoclinic phase in both compounds. A sizable electronic or Jahn-Teller effect can thus be excluded, and the intermediate distortions seem to stem from internal strain in these rotated phases.

The low-temperature crystal structure in both compounds exhibits well-defined long-range ordered rotation and tilt deformations, but evidence for some local disorder can be detected for K_2SnCl_6 in the high-temperature cubic phase just above the upper structural transition. The magnetoelastic coupling in K_2ReCl_6 can be quan-

tified by high-resolution PND studies, which reveal that the degeneracy of magnetic interaction is lifted by the triclinic distortion of the lattice.

The main conclusion about the absence of a Jahn-Teller distortion in K_2ReCl_6 is further supported by the analysis of the two materials with isoelectronic ReCl_6 groups Rb_2ReCl_6 and Cs_2ReCl_6 , in which larger alkaline ions suppress the rotational phase transitions. Indeed we do not find any evidence for such transitions, and the cubic lattice symmetry persisting to low temperatures renders a Jahn-Teller effect very unlikely also for these materials with identical electronic configuration. The magnetic properties including the occurrence of antiferromagnetic order are very similar to those in K_2ReCl_6 indicating an important impact of more distant and non-frustrated interaction parameters.

ACKNOWLEDGMENTS

We acknowledge support by the DFG (German Research Foundation) via Project No. 277146847-CRC 1238 (Subprojects A02 and B04). This work is partially based on experiments performed at the Swiss spallation neutron source SINQ, Paul Scherrer Institute, Villigen, Switzerland. We thank the ILL, Grenoble, France, for access to the D8-Venture instrument. The supporting data and codes for this article are available from Zenodo.

[1] S. Raghu, X.-L. Qi, C. Honerkamp, and S.-C. Zhang, Topological mott insulators, *Phys. Rev. Lett.* **100**, 156401 (2008).

[2] X. Zhang, H. Zhang, J. Wang, C. Felser, and S.-C. Zhang, Actinide topological insulator materials with strong interaction, *Science* **335**, 1464 (2012).

[3] J. Maciejko and G. A. Fiete, Fractionalized topological insulators, *Nature Physics* **11**, 385 (2015).

[4] S. Trebst and C. Hickey, Kitaev materials, *Physics Reports* **950**, 1 (2022).

[5] H. Takagi, T. Takayama, G. Jackeli, G. Khaliullin, and S. E. Nagler, Concept and realization of Kitaev quantum spin liquids, *Nature Reviews Physics* **1**, 264 (2019).

[6] A. Kitaev, Anyons in an exactly solved model and beyond, *Annals of Physics* **321**, 2 (2006), january Special Issue.

[7] D. I. Khomskii, *Transition Metal Compounds* (Cambridge University Press, 2014).

[8] S. V. Streltsov and D. I. Khomskii, Jahn-Teller Effect and Spin-Orbit Coupling: Friends or Foes?, *Phys. Rev. X* **10**, 031043 (2020).

[9] J. Goodenough, *Magnetism and the Chemical Bond*, Inorganic Chemistry Section / Interscience monographs on chemistry (Interscience Publishers, 1963).

[10] H. Ishikawa, T. Takayama, R. K. Kremer, J. Nuss, R. Dinnebier, K. Kitagawa, K. Ishii, and H. Takagi, Ordering of hidden multipoles in spin-orbit entangled $5d^1$ Ta chlorides, *Phys. Rev. B* **100**, 045142 (2019).

[11] D. I. Khomskii and S. V. Streltsov, Orbital Effects in Solids: Basics, Recent Progress, and Opportunities, *Chemical Reviews* **121**, 2992 (2021), pMID: 33314912.

[12] D. Khomskii and J. van den Brink, Anharmonic Effects on Charge and Orbital Order, *Phys. Rev. Lett.* **85**, 3329 (2000).

[13] Y. Weng and S. Dong, Manipulation of $J_{\text{eff}} = \frac{3}{2}$ states by tuning the tetragonal distortion, *Phys. Rev. B* **104**, 165150 (2021).

[14] B. Yuan, J. P. Clancy, A. M. Cook, C. M. Thompson, J. Greidan, G. Cao, B. C. Jeon, T. W. Noh, M. H. Upton, D. Casa, T. Gog, A. Paramekanti, and Y.-J. Kim, Determination of Hund's coupling in $5d$ oxides using resonant inelastic x-ray scattering, *Phys. Rev. B* **95**, 235114 (2017).

[15] J.-R. Soh, M. E. Merkel, L. V. Pourovskii, I. Živković, O. Malanyuk, J. Pásztorová, S. Francoual, D. Hirai, A. Urru, D. Tolj, *et al.*, Spectroscopic signatures and origin of hidden order in Ba_2MgRe_6 , *Nature Communications* **15**, 1 (2024).

[16] S. V. Streltsov and D. I. Khomskii, Jahn-Teller Effect and Spin-Orbit Coupling: Friends or Foes?, *Phys. Rev. X* **10**, 031043 (2020).

[17] Warzanowski, P. and Magnaterra, M. and Schlicht, G. and Faure, Q. and Sahle, Ch. J. and Becker, P. and Bohatý, L. and Sala, M. Moretti and Monaco, G. and Her-

manns, M. and van Loosdrecht, P. H. M. and Grüninger, M., Spin-orbit coupling in a half-filled t_{2g} shell: The case of $5d^3$ K_2ReCl_6 , *Phys. Rev. B* **109**, 155149 (2024).

[18] Y. Du, Y. Hao, X. Hao, Y. Jia, K. Sun, and Y. Xu, Magnetic properties and spin-orbit coupling-driven Jahn-Teller distortions in K_2ReX_6 (X = Cl, Br and I) with a half-filled $5d$ - t_{2g}^3 shell, *Phys. Chem. Chem. Phys.* **27**, 20699 (2025).

[19] K. Momma and F. Izumi, *VESTA3* for three-dimensional visualization of crystal, volumetric and morphology data, *Journal of Applied Crystallography* **44**, 1272 (2011).

[20] R. H. Busey and E. Sonder, Magnetic Susceptibility of Potassium Hexachlororhenate (IV) and Potassium Hexabromorhenate (IV) from 5° to 300° K, *The Journal of Chemical Physics* **36**, 93 (1962).

[21] R. H. Busey, H. H. Dearman, and R. B. Bevan, The heat capacity of potassium hexachlororhenate(IV) from 7 to 320 K. Anomalies near 12, 76, 103, and 111 K. Entropy and free energy functions. Solubility and heat of solution of K_2ReCl_6 . Entropy of the hexachlororhenate ion, *The Journal of Physical Chemistry* **66**, 82 (1962).

[22] G. P. O'Leary and R. G. Wheeler, Phase Transitions and Soft Librational Modes in Cubic Crystals, *Phys. Rev. B* **1**, 4409 (1970).

[23] R. L. Armstrong, Structural properties and lattice dynamics of 5d transition metal antifluorite crystals, *Physics Reports* **57**, 343 (1980).

[24] H. W. Willemse, C. A. Martin, P. P. M. Meincke, and R. L. Armstrong, Thermal-expansion study of the displacive phase transitions in K_2ReCl_6 and K_2OsCl_6 , *Phys. Rev. B* **16**, 2283 (1977).

[25] H. W. Willemse, R. L. Armstrong, and P. P. Meincke, Thermal expansion measurements near the antiferromagnetic phase transitions in K_2ReCl_6 and K_2IrCl_6 , *Journal of Low Temperature Physics* **26**, 299 (1977).

[26] H. G. Smith and G. E. Bacon, Neutron Diffraction Study of Magnetic Ordering in K_2ReCl_6 , *Journal of Applied Physics* **37**, 979 (1966).

[27] V. Minkiewicz, G. Shirane, B. Frazer, R. Wheeler, and P. Dorain, Neutron diffraction study of magnetic ordering in K_2IrCl_6 , K_2ReBr_6 and K_2ReCl_6 , *Journal of Physics and Chemistry of Solids* **29**, 881 (1968).

[28] A. Bertin, T. Dey, D. Brüning, D. Gorkov, K. Jenni, A. Krause, P. Becker, L. Bohatý, D. Khomskii, V. Pomjakushin, L. Keller, M. Braden, and T. Lorenz, Interplay of magnetic order and ferroelasticity in the spin-orbit coupled antiferromagnet K_2ReCl_6 , *Phys. Rev. B* **109**, 094409 (2024).

[29] A. Bertin, L. Kiefer, P. Becker, L. Bohatý, and M. Braden, Rotational phase transitions in antifluorite-type osmate and iridate compounds, *Journal of Physics: Condensed Matter* **36**, 245402 (2024).

[30] M. Cwik, T. Lorenz, J. Baier, R. Müller, G. André, F. Bourée, F. Lichtenberg, A. Freimuth, R. Schmitz, E. Müller-Hartmann, and M. Braden, Crystal and magnetic structure of $LaTiO_3$: Evidence for nondegenerate t_{2g} orbitals, *Phys. Rev. B* **68**, 060401 (2003).

[31] H. Boysen, J. Ihringer, W. Prandl, and W. Yelon, X-ray and neutron investigations of the phase instabilities in K_2SnCl_6 , *Solid State Communications* **20**, 1019 (1976).

[32] H. Boysen and A. W. Hewat, A neutron powder investigation of the structural changes in K_2SnCl_6 , *Acta Crystallographica Section B* **34**, 1412 (1978).

[33] See Supplemental Material at **** for further information about the refinements of the structural models with X-ray and neutron powder diffraction data..

[34] V. Petříček, M. Dušek, and L. Palatinus, Crystallographic Computing System JANA2006: General features, *Zeitschrift für Kristallographie - Crystalline Materials* **229**, 345 (2014).

[35] P. J. Becker and P. Coppens, Extinction within the limit of validity of the Darwin transfer equations. II. Refinement of extinction in spherical crystals of SiF_2 and LiF , *Acta Crystallographica Section A* **30**, 148 (1974).

[36] $\beta_{m1} \approx \beta_{m2} \approx 90^\circ$, $a_{m2} \times \sqrt{2} \approx b_{m2} \times \sqrt{2} \approx c_{m2}$, $a_{m1} \approx b_{m1} \approx c_{m1}$, and $a_t \times \sqrt{2} \approx c_t$, where the indices $m2$, $m1$, and t refer to the lattice parameters of the $P2_1/n$, $C2/c$, and $P4/mnc$ structural phases.

[37] K. N. Trueblood, H.-B. Bürgi, H. Burzlaff, J. D. Dunitz, C. M. Gramaccioli, H. H. Schulz, U. Shmueli, and S. C. Abrahams, Atomic Displacement Parameter Nomenclature. Report of a Subcommittee on Atomic Displacement Parameter Nomenclature, *Acta Crystallographica Section A* **52**, 770 (1996).

[38] J. Rodriguez-Carvajal, Recent advances in magnetic structure determination by neutron powder diffraction, *Physica B: Condensed Matter* **192**, 55 (1993).

[39] P. Thompson, D. E. Cox, and J. B. Hastings, Rietveld refinement of Debye-Scherrer synchrotron X-ray data from Al_2O_3 , *Journal of Applied Crystallography* **20**, 79 (1987).

[40] L. Finger, D. Cox, and A. Jephcoat, A correction for powder diffraction peak asymmetry due to axial divergence, *Journal of applied Crystallography* **27**, 892 (1994).

[41] The absorption correction is $\exp(-\Sigma R)$, where R is the radius of the cylindrical sample and Σ is the total absorption length given by $\Sigma = \frac{N_f}{v_0} f \frac{\lambda}{1.8} \sum_i c_i \sigma_{a,i}$, where N_f is the number of formula unit, v_0 the volume of the unit cell at 120 K, $f = 0.7$ the estimated powder filling, $\lambda = 1.494\text{\AA}$ the neutron wavelength (normalized to 1.8\AA), $\sigma_{a,i}$ the absorption cross section [42] of element i contained c_i times per formula unit.

[42] V. F. Sears, Neutron scattering lengths and cross sections, *Neutron News* **3**, 26 (1992).

[43] Note that in FullProf, the anisotropic ADPs are computed with the dimensionless β_{ij} parameters where the indices i, j refer to the crystallographic axis. In the manuscript, U_{ij} (in \AA^2) are reported and the following transformation is used: $U_{ij} = \beta_{ij} / (2\pi^2 a_i^* a_j^*)$, where a_i^* denote the reciprocal lattice parameters [37]. Note that when setting the Cl ADPs constraints to refine only 2 parameters, only the change of basis is considered in the β calculations, but not the small tetragonal/monoclinic splitting and monoclinic angles, the latter having only a minor impact of the order 10^{-4} on the U_{ij} values, well below the standard deviations.

[44] K. Koteras, S. Biesenkamp, P. Barone, Z. Mazej, G. c. v. Tavčar, T. C. Hansen, J. Lorenzana, W. Gochala, and M. Braden, Rearrangement of orbitals in $KAgF_3$ due to the Kugel-Khomskii mechanism: A neutron diffraction and density functional theory study, *Phys. Rev. B* **111**, 115156 (2025).

[45] A. G. Brown, R. L. Armstrong, and K. R. Jeffrey, Direct Measurement of an Order Parameter Associated with the 110.9-K Displacive Phase Transition in K_2ReCl_6 , *Phys. Rev. B* **8**, 121 (1973).

[46] P. Stein, T. C. Koethe, L. Bohatý, P. Becker, M. Grüninger, and P. H. M. van Loosdrecht, Local sym-

metry breaking and low-energy continuum in K_2ReCl_6 , *Phys. Rev. B* **107**, 214301 (2023).

[47] J. D. Dunitz, V. Schomaker, and K. N. Trueblood, Interpretation of atomic displacement parameters from diffraction studies of crystals, *The Journal of Physical Chemistry* **92**, 856 (1988).

[48] M. Braden, M. Meven, W. Reichardt, L. Pintschovius, M. T. Fernandez-Diaz, G. Heger, F. Nakamura, and T. Fujita, Analysis of the local structure by single-crystal neutron scattering in $La_{1.85}Sr_{0.15}CuO_4$, *Phys. Rev. B* **63**, 140510 (2001).

[49] W. F. Kuhs, The anharmonic temperature factor in crystallographic structure analysis, *Australian Journal of Physics* **41**, 369 (1988).

[50] R. J. Nelmes, G. M. Meyer, and J. E. Tibballs, The crystal structure of tetragonal KH_2PO_4 and KD_2PO_4 as a function of temperature, *Journal of Physics C: Solid State Physics* **15**, 59 (1982).

[51] H. T. Stokes, D. M. Hatch, and B. J. Campbell, ISOTROPY Software Suite.

[52] J. Winter, K. Rössler, J. Bolz, and J. Pelzl, Mössbauer Effect and Raman Studies of the Structural Phase Transitions in $K_2[SnCl_6]$, *physica status solidi (b)* **74**, 193 (1976).

[53] J. Pelzl, P. Engels, and R. Florian, Raman spectroscopic study of the structural phase transitions in K_2SnCl_6 , *physica status solidi (b)* **82**, 145 (1977).

[54] Y. M. Seo, J. Pelzl, and C. Dimitropoulus, Comparison of ^{35}Cl NQR Spectra between the Mixed Crystals $K_2Sn_{1-x}Re_xCl_6$ and the Al^{3+} Doped Crystals $K_2SnCl_6:Al^{3+}$, *Zeitschrift für Naturforschung A* **53**, 552 (1998).

[55] J. Ihringer, An X-ray investigation of the high-temperature phase of K_2SnCl_6 , *Acta Crystallographica Section A* **36**, 89 (1980).

[56] J. Lynn, H. Patterson, G. Shirane, and R. Wheeler, Soft rotary mode and structural phase transitions in K_2ReCl_6 , *Solid State Communications* **27**, 859 (1978).

[57] R. L. Armstrong, Structural properties and lattice dynamics of 5d transition metal antifluorite crystals, *Physics Reports* **57**, 343 (1980).

[58] W. Kugler, K. Knorr, and W. Prandl, The lattice parameters of K_2SnCl_6 at low temperatures determined by high resolution single crystal X-ray diffraction, *Solid State Communications* **47**, 163 (1983).

[59] J. Ihringer and S. C. Abrahams, Soft modes and elastic strain at the tetragonal-to-monoclinic phase transition in antifluorite and related structure types, *Phys. Rev. B* **30**, 6540 (1984).

[60] Because of the temperature offset ΔT in the PND measurements, in order to calculate the bond-distances and octahedral rotation/tilt angles, lattice parameters computed at 260 K (first refinement with a tetragonal cell) and 254 K are used in combination with the single crystal refinements at 262 K ($P4/mnc$) and 257 K ($C2/c$). At 150 K, the lattice parameters are averaged from the results obtained at 200 K and 100 K.

[61] G. Sperka and F. A. Maunter, Crystal growth and structure of Cs_2ReCl_6 , *Crystal Research and Technology* **23**, K109 (1988).

[62] B. N. Figgis, J. Lewis, and F. E. Mabbs, The magnetic properties of some d^3 -complexes, *J. Chem. Soc.* **1961**, 3138 (1961).

[63] M. Bettinelli and C. D. Flint, Magnon sidebands and cooperative absorptions in K_2ReCl_6 and Cs_2ReCl_6 , *Journal of Physics C: Solid State Physics* **21**, 5499 (1988).

[64] M. Bettinelli, C. D. Flint, G. Ingletto, M. Veterinaria, and V. Taglio, Luminescence Properties of A_2ReCl_6 Crystals, *J. Mater. Chem.* **1**, 437 (1991).

[65] M. Braden, P. Schweiss, G. Heger, W. Reichardt, Z. Fisk, K. Gamayunov, I. Tanaka, and H. Kojima, Relation between structure and doping in $La_{2-x}Sr_xCuO_{4+\delta}$ a neutron diffraction study on single crystals, *Physica C: Superconductivity* **223**, 396 (1994).

[66] A. Bertin, L. Kiefer, V. Pomjakushin, O. Fabelo, P. Becker, L. Bohatý, and M. Braden, Data and analysis codes for "Structural studies on A_2ReCl_6 ($A=K, Rb, Cs$): absence of Jahn-Teller distortion", zenodo (2026).